Magnetic diagnostic optimization for plasma equilibrium reconstruction in the HSX stellarator

Magnetic diagnostic optimization for plasma equilibrium reconstruction in the HSX stellarator

E. Chlechowitz[1], J.N. Talmadge[1], J.D. Hanson[2], F.S.B. Anderson[1] and D.T. Anderson[1]

[1] Department of Electrical and Computer Engineering, University of Wisconsin–Madison, Madison, Wisconsin 53706, USA
[2] Physics Department, Auburn University, Auburn, Alabama 36849, USA

E-mail: chlechowitz@wisc.edu

CrossMark

Abstract

A new set of 80 optimized magnetic diagnostics has been designed, built and installed in the helically symmetric experiment stellarator to enable a more accurate reconstruction of the plasma equilibrium compared to a previously installed unoptimized set. The optimization of the positions of the diagnostic coils was based on two different methods. The first technique searches for diagnostics with a high signal effectiveness. This quantity is determined by how much the variance of the reconstructed parameters, which are used to describe the equilibrium, changes depending on a change in the variance of the measurement. The results of this method are combined with a study that determines which diagnostics have the largest signal change if only a single parameter is varied. Calculations show that the new set of diagnostics reduces the uncertainty in the reconstructed plasma pressure and plasma current profile compared to the previous magnetic diagnostics and a virtual internal diagnostic set which was not optimized. With a reduction in the signal uncertainties, a further improvement can be achieved for the optimized diagnostic set, demonstrating the advantage of a careful diagnostic design process. It is shown that it is possible to design diagnostic coils which are only sensitive to either the bootstrap current or the Pfirsch–Schlüter current.

Keywords: magnetic diagnostics, optimization, plasma equilibrium reconstruction, stellarator

(Some figures may appear in colour only in the online journal)

1. Introduction

Knowledge of the basic transport and stability properties of a magnetically confined plasma depends on an accurate and reliable means of reconstructing the plasma equilibrium. Each plasma equilibrium is characterized by the plasma pressure profile, the plasma current profile and the magnetic field topology generated by currents external to the plasma. Once the equilibrium is determined, control mechanisms can be applied to adjust the plasma into a particular desired state to avoid possible plasma instabilities [1]. The challenge is in using local measurements to make conclusions about the global plasma equilibrium that are necessary to decide which control methods should be applied to obtain the preferred global and local plasma parameters.

Methods of reconstructing the plasma equilibrium for two-dimensional toroidal devices have been available for many decades. In recent years there has been substantial progress in applying reconstruction techniques to three-dimensional (3D) devices such as stellarators. Moreover, it has become clear that 3D effects are also important in tokamaks and reversed field pinches (RFP). 3D resonant magnetic perturbation (RMP) coils are now commonly used on tokamaks to suppress or excite edge localized modes (ELMs) [2, 3]. Nonaxisymmetric, non-resonant perturbations have been used to slow down or accelerate plasma rotation [4] as well as control and feedback on

kink/ballooning and resistive wall modes [5]. Departures from axisymmetry in tokamaks may occur due to asymmetrically placed test blanket modules (TBM), misaligned coils or by the addition of saddle coils [6]. In the normally axisymmetric RFP, the discovery of the improved confinement regime in the single helicity state similarly drove the physics to a fully 3D approach [7].

A summary of 3D equilibrium reconstruction results with the V3FIT code as applied to stellarators, a tokamak and an RFP is given in reference [8]. V3FIT [9] relies on the variational moments equilibrium code (VMEC) [10, 11] which assumes nested flux surfaces. The first equilibrium reconstruction of an ohmically driven current profile in a torsatron was demonstrated in the compact toroidal hybrid (CTH) device [12]. In the helically symmetric experiment (HSX), equilibrium reconstruction was used to demonstrate that the Pfirsch–Schlüter current is reduced in magnitude and rotates helically due to the lack of toroidal curvature in the device [13]. It was also shown in HSX that the bootstrap current is in good agreement with a neoclassical calculation [14]. V3FIT was applied to the RFX-mod to demonstrate that a single helicity state in an RFP can be detected using a combination of magnetic and kinetic diagnostics [15]. A similar approach to 3D equilibrium reconstruction uses the STELLOPT [16] code and has been applied to W7-AS [17] and DIII-D [18], while forward modeling of the diagnostic response was calculated for LHD [19] as well as ITER [20].

Typically in an experimental device, diagnostic placement is limited by accessibility and engineering constraints. For the forward modeling and equilibrium reconstruction, the diagnostics were not necessarily optimized to provide the most information concerning the equilibrium with the least number of diagnostics. Without optimization, the solution space calculated by minimizing the difference between the calculated and measured signal responses can often cover a broad variety of profiles as was shown on HSX [13]. Pomphrey [21] used singular value decomposition to optimize the number and location of magnetic diagnostics mounted on the exterior surface of the National Compact Stellarator Experiment. An analysis of magnetic diagnostics for equilibrium reconstruction using principal component analysis concluded that it was difficult to extract profile information for Wendelstein 7-X [22]. Hanson describes the method of signal effectiveness to determine which signals are most important in determining the profile parameters [12].

In this paper, we will describe the results of a study to determine an optimal set of internal magnetic diagnostics that reduces the uncertainty in the pressure and current profiles compared to a pre-existing set of diagnostics. We based the method of optimization on Hanson's signal effectiveness as well as a single parameter dependence study. An array of 80 magnetic diagnostics, measuring mostly the radial and poloidal components of the magnetic field, was then built and installed inside the vacuum vessel of HSX. It is shown for the first time that an optimized array can be designed and built that reduces the profile uncertainty.

In general, the parallel current that is reconstructed in a toroidal configuration may be a combination of ohmic heating,

radio frequency or beam driven current drive and bootstrap current. In HSX ohmic heating and beam driven currents are absent. Furthermore, it has been shown that the parallel current reverses direction symmetrically with a reversal of the magnetic field indicating that electron cyclotron current drive is minimal [13]. For HSX the total parallel current profile is synonymous with the bootstrap current profile, although in other experiments this may not be the case. It is shown in this paper that specific coils in the array have a high sensitivity to either the bootstrap current or the Pfirsch–Schlüter current. This ability to distinguish between these currents is especially significant to an experiment like W7-X. In that experiment the proper functioning of the edge island divertor is dependent on keeping the edge rotational transform fixed. Because the bootstrap current can impact the edge transform, it is necessary to rely on current drive or external coils to constrain the magnetic topology [23].

In this paper, section 2 describes the characterization of the plasma equilibrium at HSX. Section 3 explains the set of virtual diagnostics used in the optimization procedure to determine the locations for the new magnetic diagnostics, designed to provide more accurate plasma reconstructions. The optimization methods are described in sections 4 and 5. Section 6 describes some further technical limitations influencing the diagnostic design. The final diagnostic setup is presented in section 7. Section 8 characterizes the performance and sensitivity of the new array. Conclusions are given in section 9.

2. Plasma equilibrium characterization

The plasma equilibrium is determined through the steady-state force balance equation defined by

$$\nabla p = \vec{j} \times \vec{B} \tag{1}$$

with the plasma pressure p, the plasma current density $\vec{j}$ and the magnetic field $\vec{B}$ caused by the currents inside the plasma and external to the plasma. In this work VMEC is used to calculate the plasma equilibria.

A set of functions is available to characterize the fits to the plasma current and plasma pressure profiles. These functions are determined by the parameters k that can be adjusted during the reconstruction process to minimize χ^2 which is defined by

$$\chi^2(\underline{k}) = \sum_i w_i \left(\frac{S_{\text{meas},i} - S_{\text{cal},i}(\underline{k})}{\sigma_i} \right)^2, \tag{2}$$

and represents the sum of the discrepancy between the measured signals S_{meas} and the predicted diagnostic responses S_{cal} based on the calculated plasma equilibrium. w_i and σ_i are the weight and measured signal uncertainty of each diagnostic i, respectively. The number of free parameters depends on the desired flexibility to cover the range of expected equilibria. However, for several reasons, the functions should be defined with the fewest parameters necessary. With each new parameter the computational time is increased. Furthermore, it may also increase the number of local minima of χ^2. Thus, the probability that the reconstruction does not finish in a global
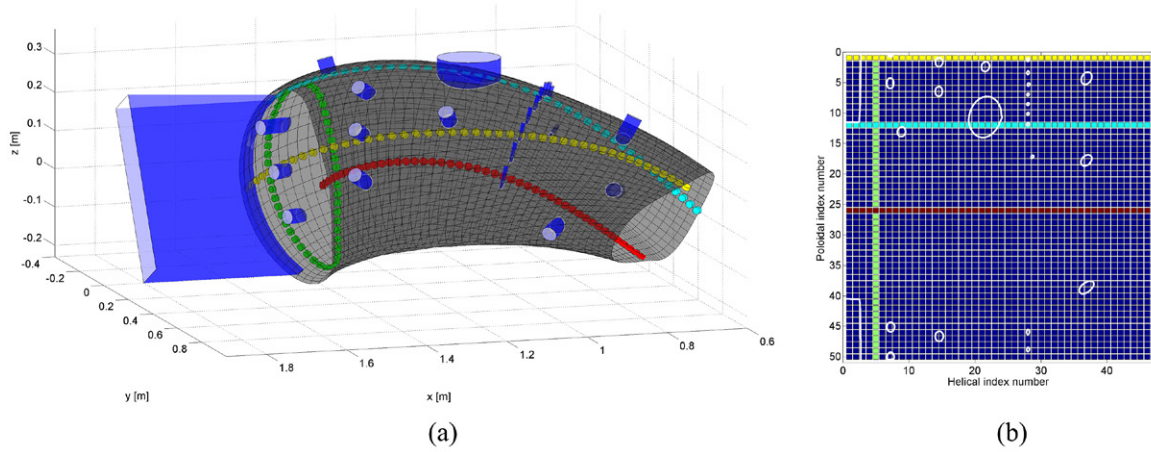
Figure 1. Location of virtual diagnostics is expressed by two indices. Mapping is illustrated for three subsets of diagnostics (yellow, cyan and red) with the same poloidal index number (1, 12 and 26) and one subset (green) with the same helical index number (5). (*a*) Subset of virtual diagnostics (green, yellow, cyan, red) inside a half field period (change in the toroidal angle of $\pi/4$) of the HSX vessel. (*b*) Diagnostics are mapped on a 2D grid using a helical and poloidal index number.

minimum is higher. The risk that V3FIT does not converge to a global minimum is increased if different combinations of parameter values would lead to similar profiles.

Prior work [24] has shown that for central peaked pressure profiles, the function given by

$$p(s) = \frac{\text{PRESSCALE}}{1 - f_p(s = 1)}[f_p(s) - f_p(s = 1)] \qquad (3)$$

with

$$f_p(s) = \left(1 + \left(\frac{s}{(AM_2)^2}\right)^{AM_3}\right)^{-1} \qquad (4)$$

provides good coverage through the variation of the parameters AM_2, AM_3 and PRESSCALE of the measured profiles at HSX using a Thomson scattering diagnostic. AM_2 and AM_3 describe the width and steepness of the pressure profiles, respectively. The parameter PRESSCALE scales the pressure profile and its value is associated with the pressure on the magnetic axis. s represents the normalized toroidal flux coordinate. To cover pressure profiles with multiple gradient regions, a more general expression of the pressure profile may be needed with additional free parameters.

The plasma current profile is characterized by

$$I(s) = \text{CURTOR} \cdot \frac{f_I(s)}{f_I(s = 1)} \qquad (5)$$

with

$$f_I(s) = \frac{2}{\pi}\text{atan}\left(\frac{AC_2 \, s^{AC_3}}{1 - s}\right). \qquad (6)$$

By varying AC_2 and AC_3 a good trade-off between the flexibility of the profile and number of free parameters is provided [24]. CURTOR characterizes $I(s = 1)$, which is the total enclosed current. AC_2 and AC_3 express the steepness and width of the peak in the function, respectively. For $AC_3 < 1$ the current density is singular at $s = 0$. However, for the equilibrium calculation VMEC uses a profile of the

total enclosed plasma current which is generally bounded to be zero on the axis. Because the bootstrap current is strongly dependent on the density and temperature gradient, the possible current profiles, given by equations (5) and (6), encompass a range of profiles that are compatible with the density and temperature derivative. To encompass current density profiles that are not unidirectional, for example when local regions of the bootstrap current density are in the opposite direction or in the current evolution phase when shielding currents exist [14], additional free parameters may be required.

3. Virtual diagnostic set

A grid of small virtual diagnostics has been generated to determine the best local positions for new diagnostics. Due to stellarator symmetry, the diagnostics cover only one half of a field period in HSX. The center of the virtual diagnostics is located approximately 1 cm away from the inside of the vessel, so that the diagnostics are not in contact with the plasma. Each grid point has three virtual diagnostics. One, which is referred to as a radial direction, measures a magnetic field component that is perpendicular to the vessel. The second diagnostic has a normal vector which follows a helical path that makes two poloidal rotations for one toroidal rotation. The third diagnostic is perpendicular to the other two and measures a poloidal-like magnetic field component.

The location of the diagnostics is determined by two indices, one for a poloidal-like direction and one for a helical-like direction. The mapping is illustrated in figure 1. Here, a set of 50 diagnostics (green) with the same helical index number '5' that lie close to the rectangular box port and 3 sets of 46 diagnostics (yellow, cyan and red) with the same poloidal number (1, 12 and 26) which follow the helical contour are mapped to a 2D coordinate system. The vacuum vessel ports are also projected and indicated as white circles or rectangles.

Table 1. Parameter range used to calculate a set of equilibria for the signal effectiveness study.

Parameter name	Range
CURTOR	50–450
AC_2	5–15
AC_3	0.8–1.2
PRESSCALE	100–1000
AM_2	0.19–1.26
AM_3	0.475–3.15

Table 2. Parameter values used to calculate a set of equilibria for the single parameter dependence study.

Parameter name	Values
CURTOR	0, 100, 200
AC_2	5, 10, 15
AC_3	0.8, 1.0, 1.2
PRESSCALE	0, 500, 1000
AM_2	0.2, 0.4, 0.6
AM_3	0.5, 1.0, 1.5

4. Signal effectiveness study

One opportunity to find the most important diagnostics for plasma equilibrium reconstruction was recently proposed [12]. A quantity which is referred to as signal effectiveness was introduced. It describes which signals or measurements have a strong impact on the determination of each reconstruction parameter k. It is defined by

$$E_{kl} \equiv \frac{\sigma_l^{S_{\text{meas}}}}{\sigma_k^P} \frac{\mathrm{d}\, \sigma_k^P}{\mathrm{d}\, \sigma_l^{S_{\text{meas}}}}. \tag{7}$$

where E_{kl} is dimensionless and represents the ratio of the fractional reduction of the k-th parameter variance to the fractional reduction in the variance of the l-th measured signal. Here, $\sigma_l^{S_{\text{meas}}}$ is the square root of the variance of the measured signal. σ_k^P represents the square root of posterior covariance of a reconstruction parameter. Thus, σ_k^P describes the uncertainty in the value of the determined parameter.

For the set of 1379 test equilibria, the signal effectiveness has been calculated for the virtual diagnostics described in section 3. For all of these equilibria calculations, 6 poloidal modes, 8 toroidal modes and 50 flux surfaces have been used in VMEC. Extensive sensitivity tests were performed to confirm that the equilibria were adequately converged [25]. The set of equilibria which vary in the plasma current profile and plasma pressure profile have been generated for the parameter range listed in table 1.

The signal effectiveness calculation yields a three-dimensional matrix with the components E_{klm} where k stands for the different reconstruction parameters, l for the index of the diagnostic and m for the index of the equilibria. These calculations have been separately performed for the radial, poloidal and helical diagnostics due to computational restrictions. For each diagnostic and reconstructed parameter an average of the signal effectiveness over all test equilibria

$$\bar{E}_{kl} = \frac{\sum\limits_{m}^{1379} E_{klm}}{1379} \tag{8}$$

has been calculated. The results for a subset of the parameters for the radial and poloidal diagnostics are shown in figures 2–4. It should be noted that the colorbar scale for the radial and poloidal diagnostics for each parameter is the same.

The signal effectiveness for different parameters k for the same diagnostic cannot be directly compared because the E_{kl} values are normalized so that the sum over all diagnostics

l is set to one. However, if the maximum value of all $\bar{E}_{k=k_1,l}$ (specific parameter k_1) is larger than the maximum value of all $\bar{E}_{k=k_2,l}$, the overall signal effectiveness is more equally distributed for k_2. An absolute statement cannot be given regarding the effectiveness of a specific diagnostic for a specific parameter, only a relative prediction compared to other diagnostics. As an example, both the radial and poloidal diagnostics have a small region with a high $\bar{E}_{kl}$ for the parameter PRESSSCALE, whereas the diagnostic location for AC_3 is not so constraining. Thus, possible locations for placing diagnostics to reconstruct PRESSCALE efficiently is more limited than for AC_3.

For most parameters (except CURTOR) the pattern of $\bar{E}_{kl}$ for the radial and poloidal diagnostics is similar but slightly poloidally and helically shifted. This behavior offers the opportunity to use diagnostic arrays of a limited size for effective measurements of both the radial and poloidal magnetic field. Furthermore, measurements can be performed in regions with different values of $\bar{E}_{kl}$ to benchmark the effectiveness of the diagnostics.

5. Single parameter dependence study

By analyzing the results from section 4, some of the reconstruction parameters showed a high signal effectiveness in different regions in the 2D diagnostic location plot. Using equation (7), a change in a diagnostic measurement performed in one of these regions would affect the reconstruction of the specific parameter more strongly than in areas with a low signal effectiveness. However, it is still unclear which of these many regions would change if the parameter changed only in a specific way. Knowledge that specific constraints for some of the reconstruction parameters exist (e.g. due to physical limitations) may result in only some areas with a high signal effectiveness being impacted by a parameter change.

Thus, a scan of each parameter keeping the other parameters constant has been performed. Since this scan shows the single parameter dependence (SPD) on each diagnostic, the results can be combined with the outcome from section 4. As a starting point the most likely equilibrium for a standard HSX discharge has been used [24]. Each parameter was then varied three times and for each case the signal responses have been calculated using the V3POST code [26]. The different parameter values are listed in table 2.

Thus, a set of 729 equilibria has been generated. It can also be interpreted that 243 equilibria EQ_i were calculated and for each of these equilibria one parameter was varied three
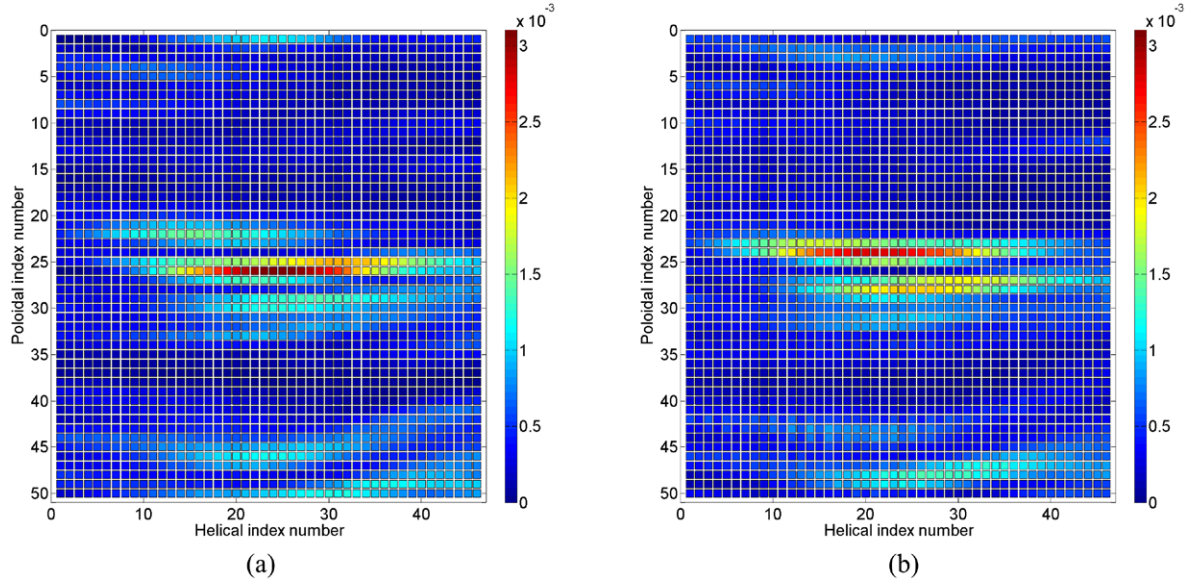
Figure 2. Average signal effectiveness for the virtual radial and poloidal magnetic diagnostics for the reconstruction parameter PRESSCALE, describing the pressure on the magnetic axis. (*a*) Radial diagnostics. (*b*) Poloidal diagnostics.
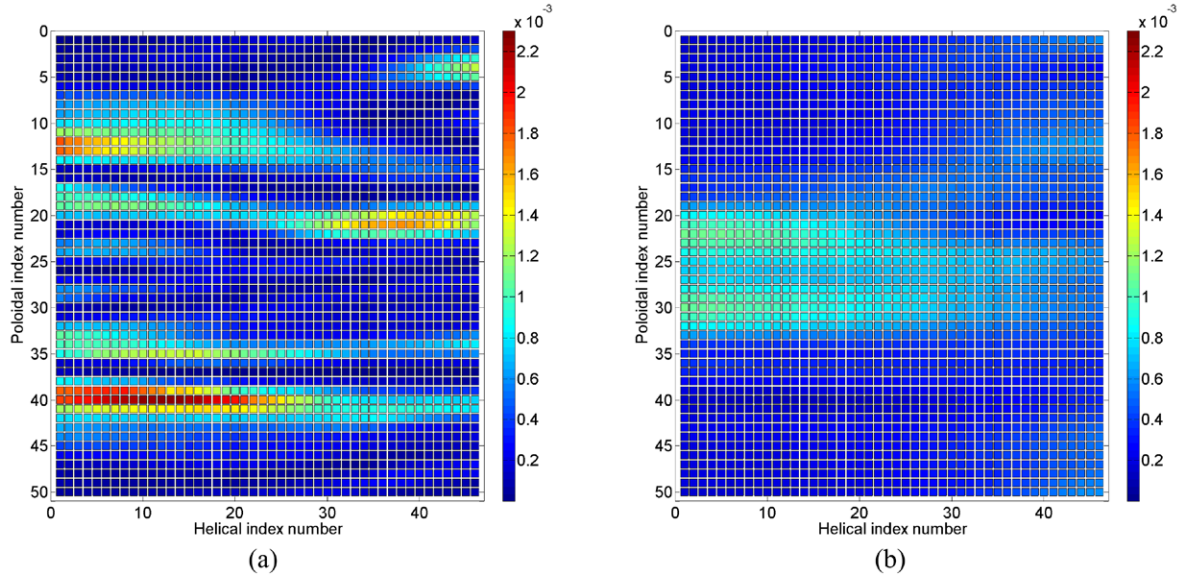

Figure 3. Average signal effectiveness for the virtual radial and poloidal magnetic diagnostics for the reconstruction parameter CURTOR, describing the enclosed plasma current. (*a*) Radial diagnostics. (*b*) Poloidal diagnostics.

times ($EQ_{i_{a,b,c}}$). The variance of the signal responses S, where five of the six parameters were constant and only one was varied, has been determined. An average of these 243 variance calculations

$$q_{\text{SPD},j} = \frac{\sum\limits_{i}^{243} \text{var}[S_j(EQ_{i_a}), S_j(EQ_{i_b}), S_j(EQ_{i_c})]}{243} \quad (9)$$

has been performed for all diagnostics j and all parameters. The results are shown in figures 5–7. The colorbar scale for the radial and poloidal diagnostics for each parameter is the same so that both diagnostic sets can be directly compared. The radial diagnostics show a larger signal change as compared to the poloidal diagnostics from varying the

reconstruction parameters which determine the pressure profile (PRESSCALE, AM_2 and AM_3). However, the poloidal diagnostics show a larger amplitude change when the plasma current is varied.

The diagnostics most affected by changing the pressure profile (through a change in the PRESSCALE parameter) shown in figure 5(*a*) can be connected to a change in the Pfirsch–Schlüter currents which are determined by the pressure profile. The Pfirsch–Schlüter currents, calculated with VMEC, have a helical dipole character for HSX [13] which is shown for two vertical cuts in figure 8. This dipole character leads to an increase in the radial magnetic field at the diagnostics in the vicinity of the indicated arrows. Thus, if the plasma pressure changes, a relatively large signal change is expected
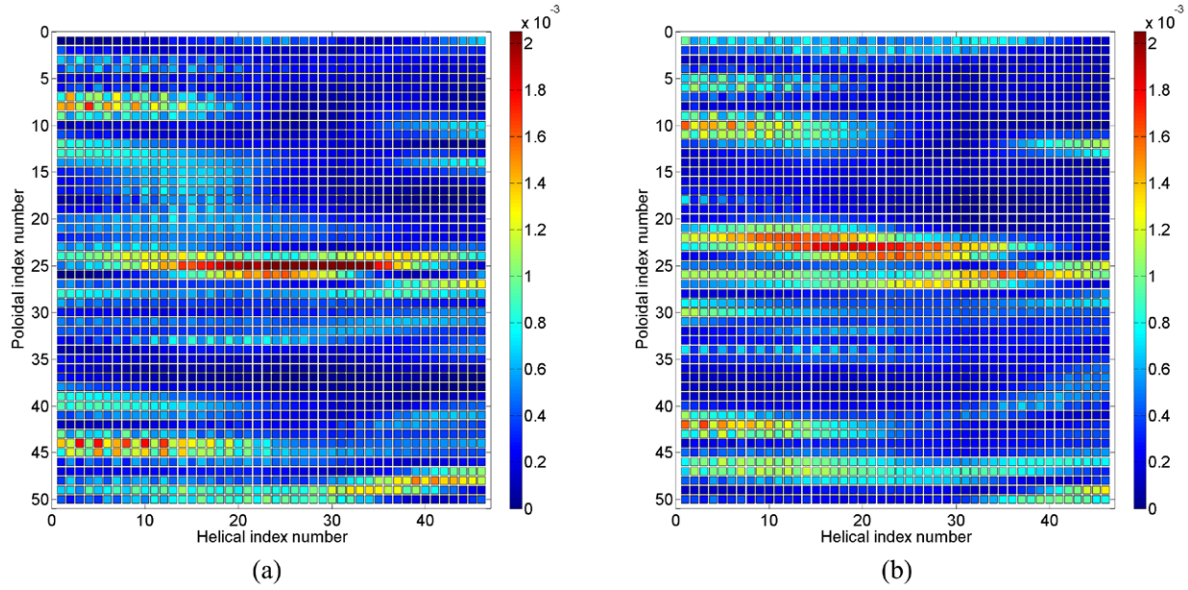
Figure 4. Average signal effectiveness for the virtual radial and poloidal magnetic diagnostics for the reconstruction parameter AC_3, describing the location and peaking of the plasma current density. (*a*) Radial diagnostics. (*b*) Poloidal diagnostics.
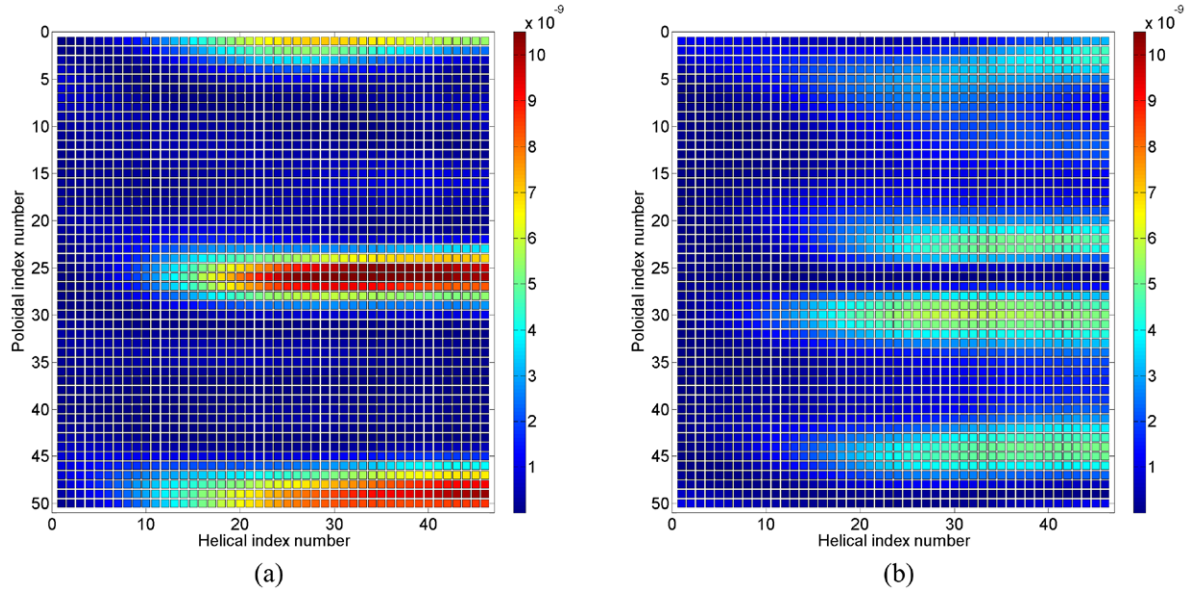

Figure 5. Average signal variance $[T^2]$ for the virtual radial and poloidal magnetic diagnostics by only varying PRESSCALE, describing the pressure on the magnetic axis. (*a*) Radial diagnostics. (*b*) Poloidal diagnostics.

for these diagnostics. Figure 8(*a*) shows radial diagnostics with a helical index 37–43 and figure 8(*b*) shows diagnostics with a helical index 1–7. The red and blue diagnostics indicate poloidal index 49 and 26, respectively. Thus, for figure 8(*a*), it can be seen that these diagnostics lie in an area where large signal changes are expected. This is confirmed by the results shown in figure 5(*a*). Conversely, for the vertical cut in figure 8(*b*), a reduced sensitivity is expected which can also be confirmed with figure 5(*a*). In figure 8(*b*) the largest effect of the Pfirsch–Schlüter currents would be expected on the upper and lower diagnostics with respect to the *z*-axis. However, the distance of these particular diagnostics to the magnetic axis and thus to the maximum of the dipole moment is a factor of approximately two larger compared to the sensitive

diagnostics shown in figure 8(*a*). Thus, the maximum signal change of diagnostics with a small helical index (when the plasma has a large elongation) is expected to be smaller than for diagnostics with a high helical index (when the plasma has a high triangularity).

By comparing the radial and poloidal diagnostics, a different area of influence (diagnostic locations) can be seen for changing a specific reconstruction parameter. This is the case for all investigated reconstruction parameters. However, by changing different parameters of the plasma pressure profile, the same radial diagnostics are affected. This is also true for the poloidal diagnostics although the signal variance for the pressure profile is not shown due to space limitations. Analogous statements can be made for the radial and poloidal
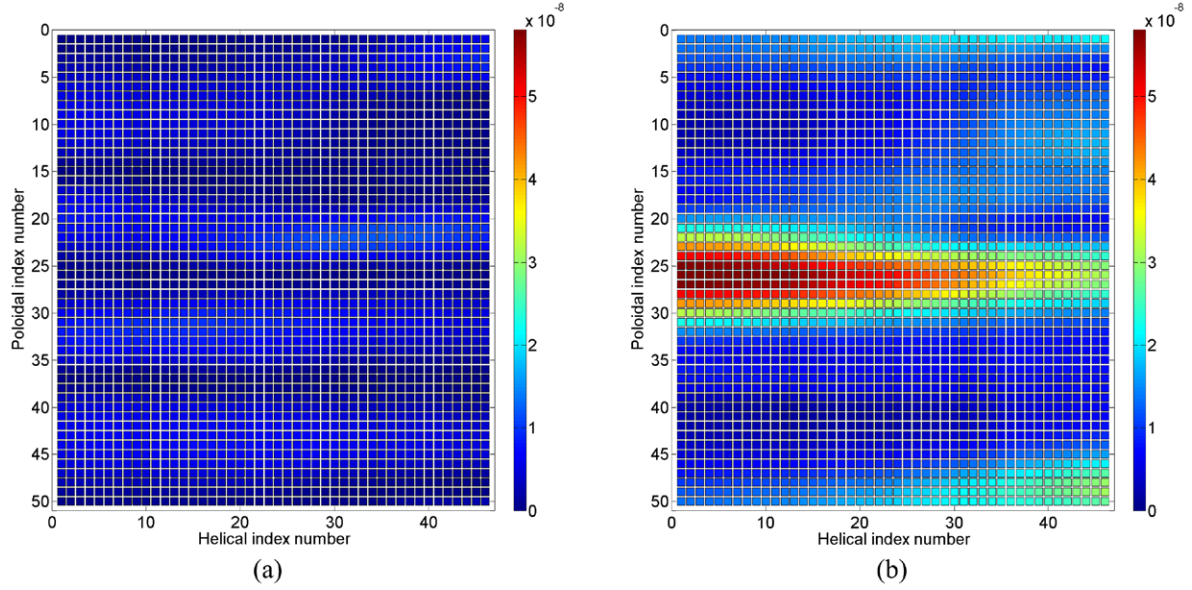
Figure 6. Average signal variance [T^2] for the virtual radial and poloidal magnetic diagnostics by only varying CURTOR, describing the enclosed plasma current. (*a*) Radial diagnostics. (*b*) Poloidal diagnostics.
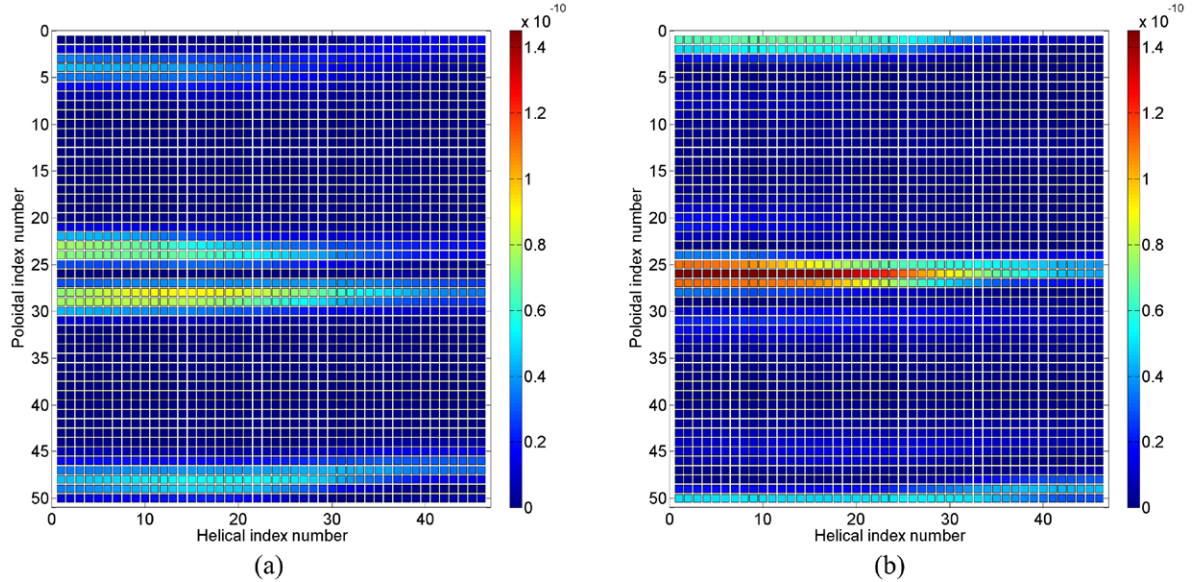

Figure 7. Average signal variance [T^2] for the virtual radial and poloidal magnetic diagnostics by only varying AC_3, describing the location and peaking of the plasma current density. (*a*) Radial diagnostics. (*b*) Poloidal diagnostics.

diagnostics if the parameters determining the current profile are varied by keeping the total current constant.

This investigation shows that the regions of influence (in diagnostic space) overlap when varying different reconstruction parameters. However, a comparison of these results with the results from section 4 indicates that not all locations which have a high signal effectiveness undergo a significant signal change. This allows a reduction in the pool of possible diagnostics.

The average signal amplitude of the helical diagnostics compared to the radial and poloidal diagnostics was found to be smaller by about a factor of 3 and 6, respectively. Thus, the signal-to-noise ratio is smallest for these diagnostics, which had previously been confirmed by existing diagnostics measuring a helical/toroidal field component. Consequently,

their contribution to the plasma equilibrium reconstruction was small [24]. The measurement uncertainty of the existing helical diagnostics was also larger than the value for the radial and poloidal diagnostics. This was mainly caused by the stronger impact from the ripple in the main magnetic field coil current. For these reasons, magnetic diagnostics measuring a helical field component are not considered for the new set of diagnostics used for plasma equilibrium reconstruction.

6. Technical constraints

Due to the limited access through ports to the inside of the vacuum vessel, the possibility to measure the diagnostic location and orientation in the vessel is restricted. Since the
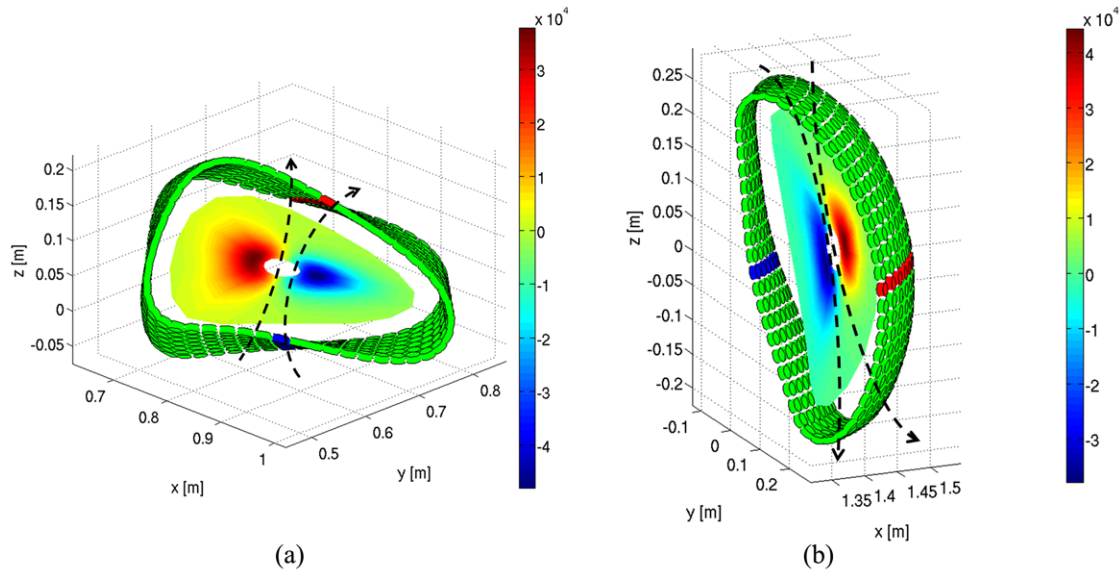
Figure 8. Pfirsch–Schlüter current density for two different vertical cuts with different sets of radial diagnostics; blue and red diagnostics have poloidal index 26 and 49, respectively. (*a*) Vertical cut through plasma close to joint flange, diagnostics have helical index number 37 to 43. (*b*) Vertical cut through plasma close to box port, diagnostics have a helical index number of 1 to 7.

location of the main magnetic field coils is known very precisely, the location of the new diagnostics can be determined with respect to the main magnetic field. However, this method requires that the relative location of the diagnostic coils to each other needs to be known very well. Thus, the whole array must be pre-assembled and measured using a portable coordinate measuring machine outside the vessel. To insert the final array into the vessel through a port, the dimensions of the whole construction are restricted.

Considering the results from sections 4 and 5, the diagnostic array should cover regions of a high signal effectiveness as well as a high expected signal change when a change in the equilibrium appears. Through an evaluation of these requirements and the technical limitations an array was chosen which covers the region where the poloidal index number ranges from about 20–35 and the helical index number is 20–30.

7. Diagnostic setup

An overview of the completed diagnostic design is shown in figure 9. All the in-vacuum components follow the internal vessel contour.

To increase the clearance between the last closed flux surface and the diagnostic, the height of the winding area for the coils measuring the poloidal magnetic fields has been made smaller compared to that of the coils measuring the radial magnetic field. The poloidal and radial coils have an area per winding of about $1.05\,cm^2$ and $2.55\,cm^2$, respectively. 132 and 120 windings exist on each poloidal and radial coil, respectively[3]. To prevent surface currents, the bobbins were built out of Macor® which has an electrical volume resistivity higher than $10^{16}\,\Omega$ cm at 25 °C. A bobbin is shown in figure 10. All coils are absolutely calibrated with a set of Helmholtz coils.

[3] The last coil in each array has 168 windings in the radial direction.
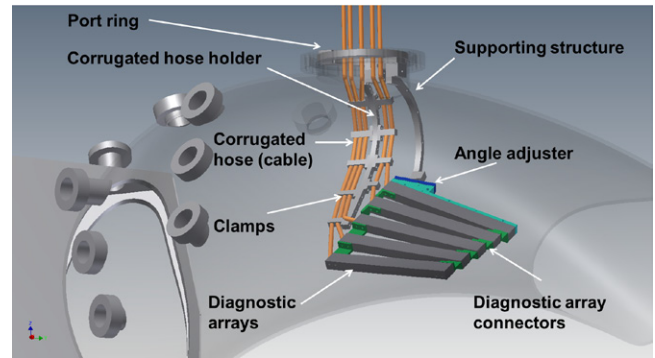

Figure 9. Complete setup of the newly built diagnostic for plasma equilibrium reconstruction.

Each coil array is enclosed in a stainless steel shell to shield the coils from the ECRH microwaves and the plasma. The plasma and vessel facing sides of the shell are 1.6 mm thick. The sides have an increased thickness of 3.2 mm due to the overlap of the two u-channels used for each array. The stainless steel framework as well as the coils in one open array are shown in figure 11. The relative positions and orientations of the diagnostic arrays have been adjusted using the distance holders (green elements in figure 9), so that they follow the vessel contour. The five arrays are connected to a supporting structure which is attached to an expandable port ring. The ring fits tightly against the inside of the port tube and acts as the anchor for the supporting structure.

The wires from the coils are enclosed in flexible stainless steel hoses which connect to the flange. The tubes are held by a cable tree structure which is also connected to the port ring. Each diagnostic array has its own 50 pin electrical feedthrough connector at the flange which would allow fast replacement if repairs or improvements were necessary. The five diagnostic arrays were pre-assembled and their relative location was measured using a portable coordinate
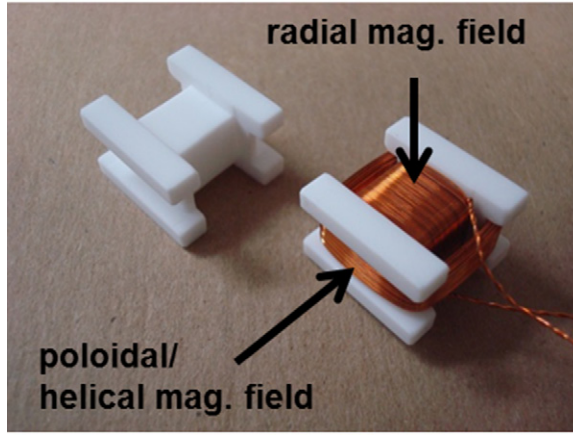
Figure 10. Bobbin used for winding the coils measuring the radial and poloidal (or toroidal) magnetic field.
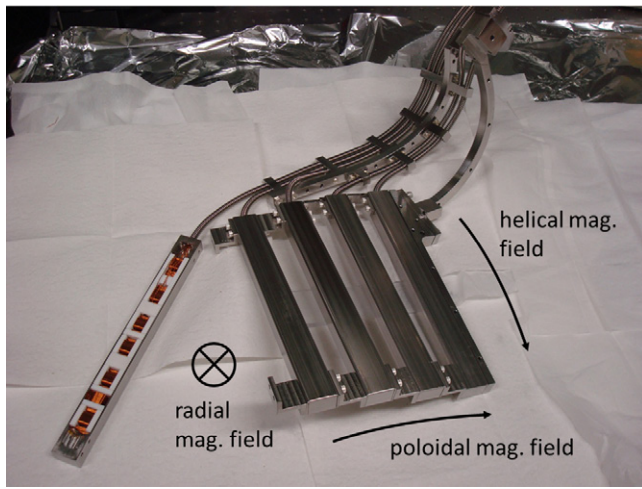

Figure 11. Diagnostic set with four closed arrays and one open array.

measuring machine outside the vessel. The diagnostic array assembly was moved though the rectangular box port and then connected to the port ring. The arrangement of the different magnetic coils inside the arrays is shown in figure 12. The five arrays are labeled A–E, with A being the nearest to the flange/port ring. The coils are numbered 1–8 with 1 being the coil closest to the corrugated tubes. The complete diagnostic set contains 39 radial coils, 38 poloidal coils and 3 helical coils. The 3 helical coils are only used to find the relative location of the diagnostic with respect to the main magnetic field.

8. Diagnostic performance and sensitivity

The performance of the newly designed diagnostic set is compared to the calculated performance of the set of previously installed diagnostics and a reference set of arbitrarily placed virtual diagnostics. The performance improvement is determined by the reduction of possible equilibria that fulfill

$$\chi_{\mathrm{red}}^2 = \frac{\chi^2}{\nu} \leqslant 1 \qquad (10)$$
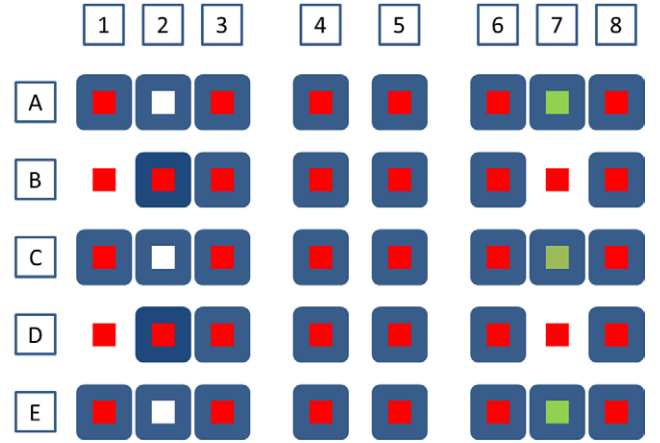
Figure 12. Orientation of the new diagnostic coils; A–E refers to the array label and 1–8 describes the position of each coil within the array.

with ν being the number of degrees of freedom. Only 50 of the 80 newly installed diagnostics are used in this section (25 radial and 25 poloidal coils). The first comparison set, given by the previously installed diagnostics, contains 15 internal magnetic coils, measuring mainly the poloidal magnetic field, as well as 32 poloidal and 32 radial diagnostics placed outside the vessel [24]. The second comparison set, which is referred to as the reference set, comprises 50 virtual coils (also 25 internal radial and 25 internal poloidal in a similar array as for the installed set). However, the location of this set was not optimized and was chosen arbitrarily. The distance between the plasma and the reference set is same as for the newly built diagnostic set. This allows the separation of the improvement due to a diagnostic location optimization from the effect of having diagnostics closer to the plasma. All investigated diagnostic sets are shown in figure 13.

A parameter scan has been performed where 5 of 6 parameters that are usually used in the reconstruction process have been varied. The number of variations are listed in table 3. The resulting equilibria are compared against a reference equilibrium which is the most likely equilibrium for a standard 50 kW heated QHS discharge at HSX [24].

The reconstruction parameter CURTOR was not varied since in prior tests this parameter could be reconstructed with sufficient accuracy. For each diagnostic set, the expected signal responses for 759 375 ($=15^5$) equilibria have been calculated to determine the χ_{red}^2 value as indicated in figure 14.
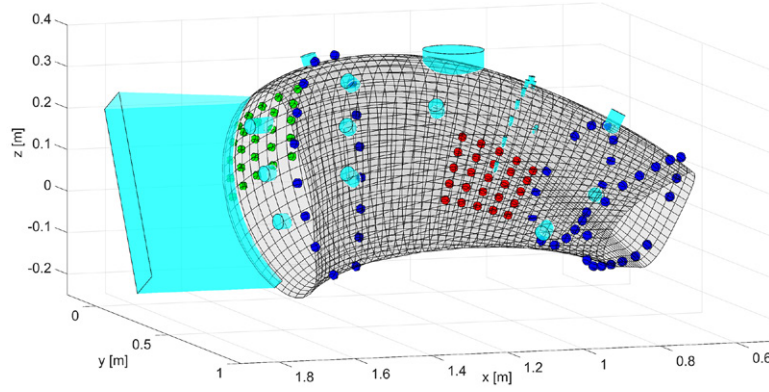
Figure 13. Set of existing magnetic diagnostics (blue) and virtual reference diagnostic set (green) have been used to test the performance of the newly built and optimized diagnostic set (red).
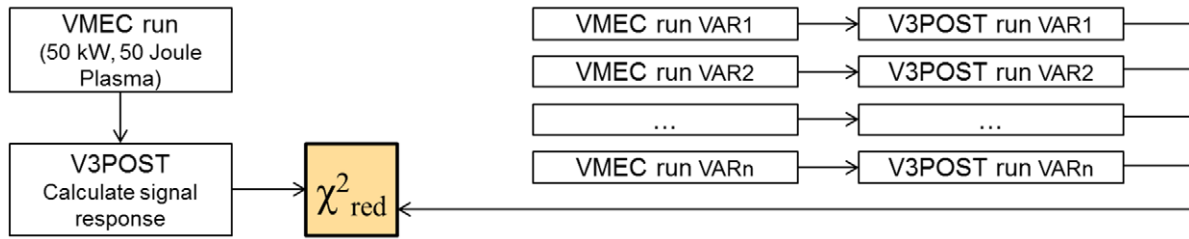

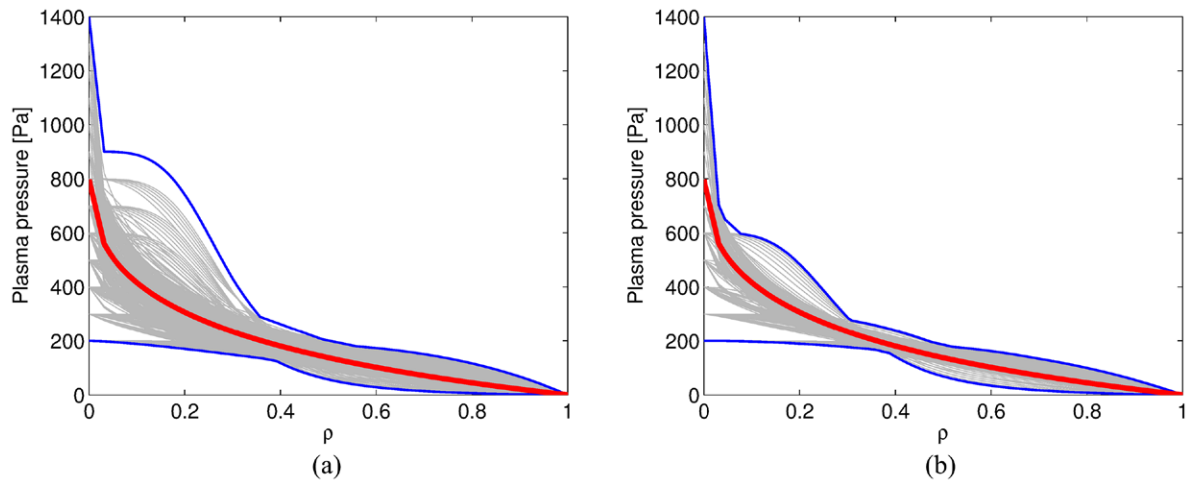**Figure 14.** Schematic parameter scan and calculation of χ^2_{red}.

Figure 15. Plasma pressure profiles fulfilling $\chi^2_{\text{red}} \leqslant 1$ for $\sigma = 0.01$ mT (gray), red curves represent the reference equilibrium, blue curves display the envelope. (*a*) Solutions using the existing magnetic diagnostics. (*b*) Solutions using the new magnetic diagnostics.

Table 3. Parameter range used to investigate the solution space to test the performance of the new set of diagnostics.

Parameter name	Range	Value reference equilibrium
AC_2	4–16	9.98
AC_3	0.01–2	1.50
PRESSCALE	0–1400	797
AM_2	0.01–4	1.0
AM_3	0.01–2	0.252

The calculations have been performed on the University of Wisconsin Computer-Aided Engineering Condor system. A total computation time of approximately 24 000 CPU hours was necessary.

A standard deviation σ of 0.01 mT was used for all diagnostics based on the experience in prior work [24]. This value describes the uncertainty in the measurement based on a possible error in the location and orientation of the coil as well as the expected noise in the measurement.

For the existing magnetic diagnostics, 20 690 cases ($\approx 2.7\%$) have been found with a χ^2_{red} smaller or equal to unity. The number of solutions for the reference diagnostic set is reduced by approximately 20 percent (16 531 cases $\approx 2.2\%$). However, for the new set only 2962 cases exist where $\chi^2_{\text{red}} \leqslant 1$ ($\approx 0.4\%$). This is a reduction of solutions by a factor of approximately
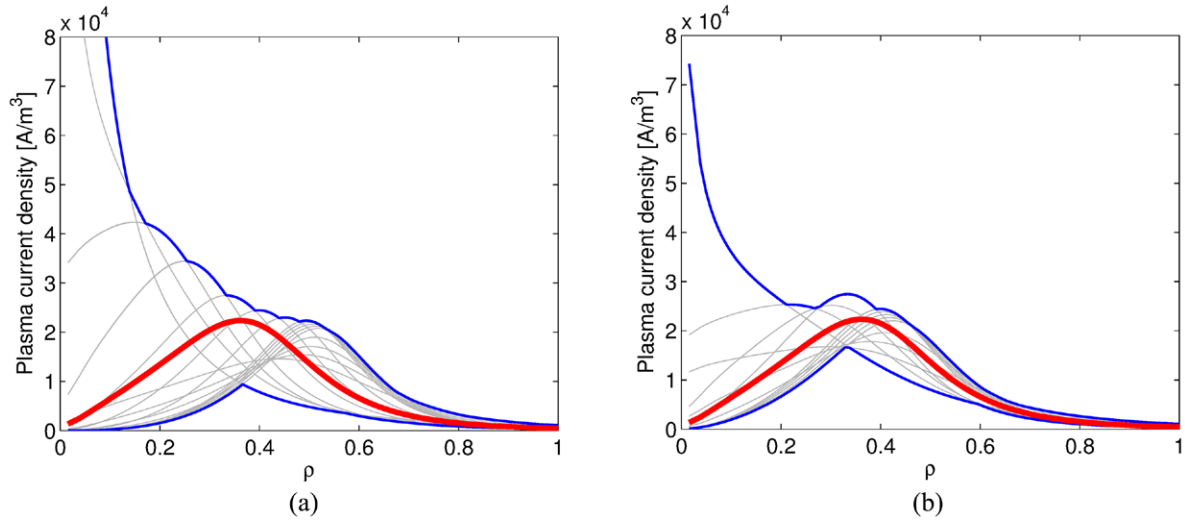
Figure 16. Plasma current density profiles fulfilling $\chi^2_{\text{red}} \leqslant 1$ for $\sigma = 0.01$ mT (gray), red curves represent the reference equilibrium, blue curves display the envelope. (*a*) Solutions using the existing magnetic diagnostics. (*b*) Solutions using the new magnetic diagnostics.
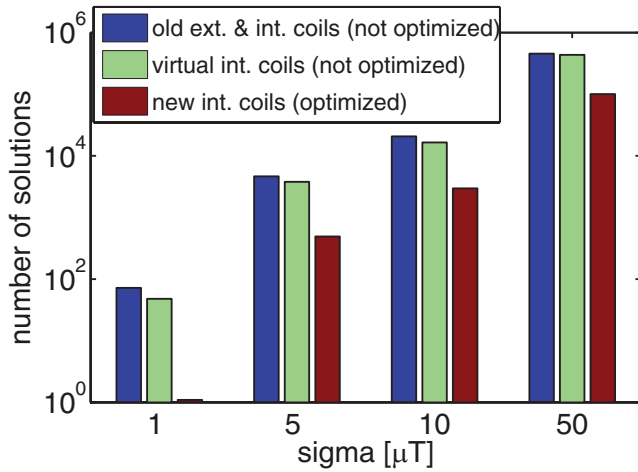

Figure 17. Number of solutions ($\chi^2_{\text{red}} \leqslant 1$) out of set of about 760 000 equilibria for different values of the signal uncertainty σ.

seven. The plasma pressure profiles and plasma current density profiles related to each set of solutions for the existing diagnostics are shown in figures 15(*a*) and 16(*a*) and for the new diagnostic set are shown in figures 15(*b*) and 16(*b*). The profiles are plotted versus the normalized radius $\rho = r/r_a$ where r_a represents the radius at the plasma boundary.

It can be seen that the existing diagnostics allow solutions with profiles that differ significantly from the reference QHS equilibrium case. The range of variation is much more limited for the new diagnostic set.

If the uncertainty in the measurement σ is reduced, an additional reduction of possible solutions can be achieved as seen in figure 17. For this reason the new set of diagnostics was measured outside of the vessel to reduce the uncertainty in the relative location and orientation of the diagnostics to each other.

A demonstration of the sensitivity for a subset of the new diagnostic coils with respect to specific reconstruction parameters is shown. The plasma used for this sensitivity
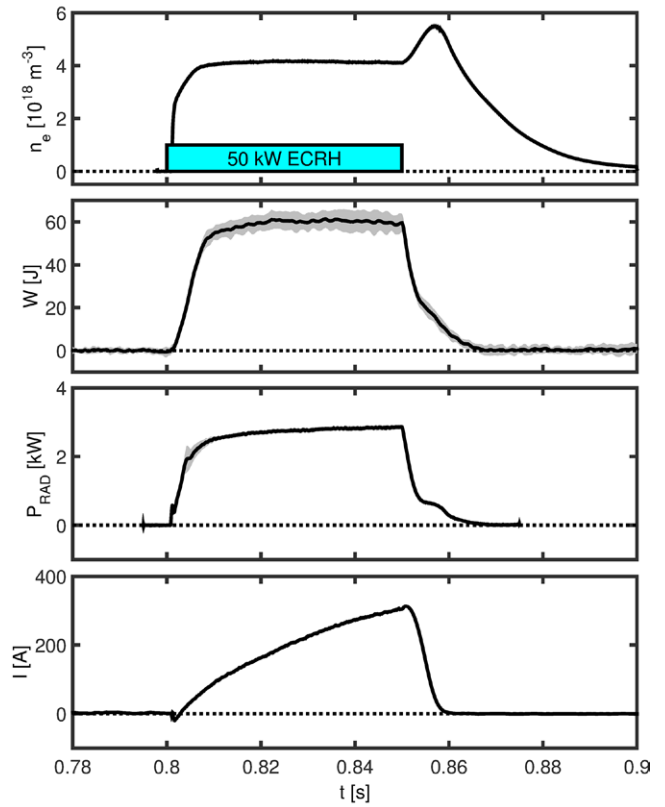

Figure 18. Time traces for investigated plasma, from top to bottom: line-averaged electron density, stored energy, radiated power, plasma current.

demonstration was generated with 50 kW ECRH at a frequency of 28 GHz. The magnetic field on axis was 1.0 T so that the polarization of the ECRH wave was chosen to be parallel to the main magnetic field (ordinary mode heating at the fundamental harmonic). The time traces for the line-averaged density, the plasma energy, the radiated power, and the plasma current are shown in figure 18. These traces represent the average signal of eleven similar plasma discharges. The
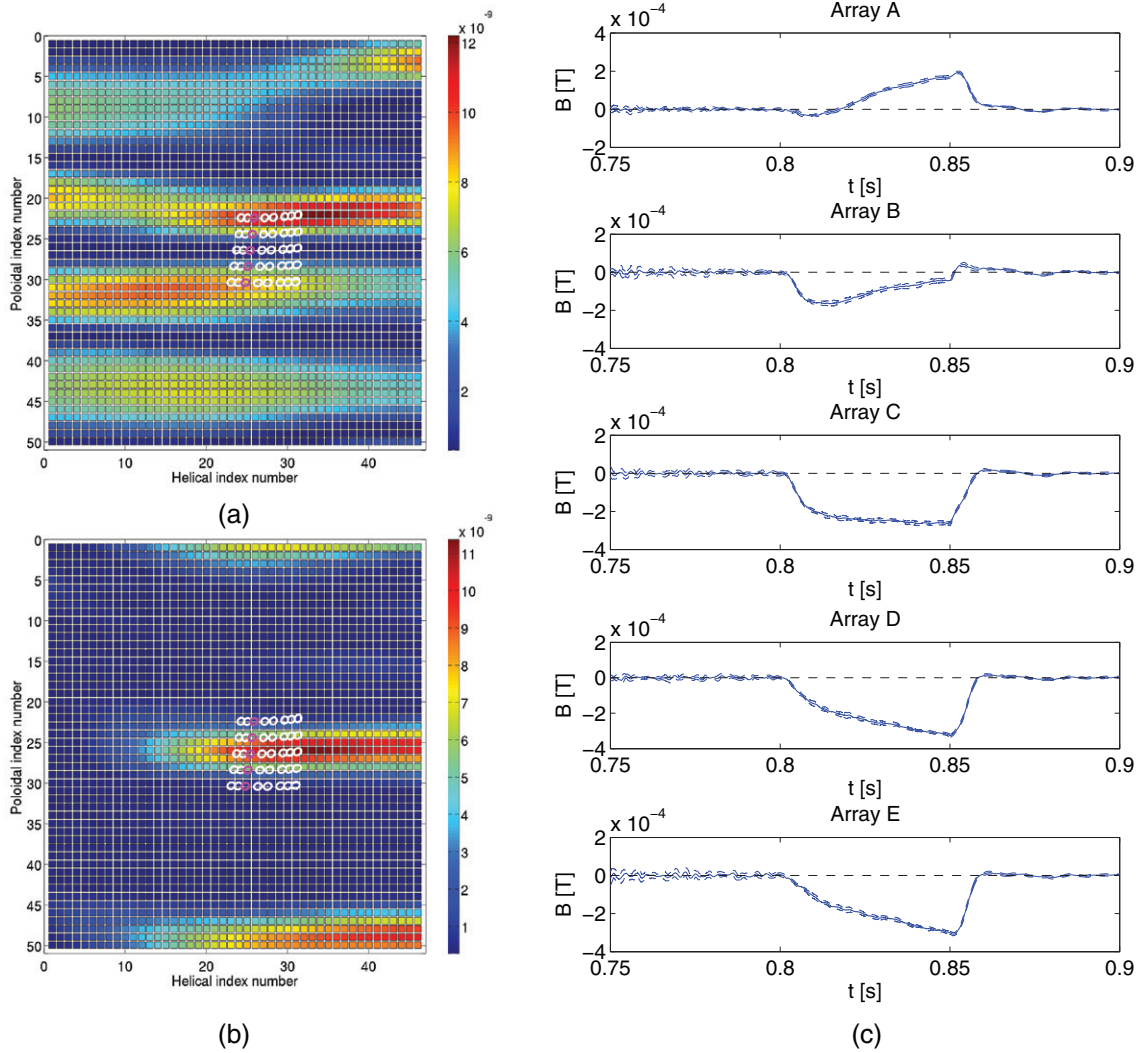
Figure 19. Results from the Single Parameter Dependence Study (section 5) for diagnostic coils measuring a radial magnetic field indicating which coil would show a signal change if only the plasma current changes (*a*) or only the plasma pressure (*b*). The magnitude of the change is correlated with the color scale. (*c*) Measurements of the coils, which locations are marked as magenta colored circles in (*a*) and (*b*), show different temporal behavior caused by the different equilibrium currents; dashed lines represent standard deviation from 11 similar discharges.

interferometer measurements indicate that the plasma breakdown occurred at 0.801 s. A constant line-averaged density of $4.1 \cdot 10^{18}\,m^{-3}$ has been achieved for the time period from 0.81 s to 0.85 s. The plasma current is rising throughout the whole discharge with a maximum of about 312 A.

As an example, the signals of five coils measuring the radial magnetic fields are investigated. These coils are wound on the third bobbin within each of the five arrays. Figures 19(*a*) and (*b*) show the location of all coils, which are indicated as circles, on a 2D map of possible diagnostic locations, introduced in section 3. The locations of the five coils investigated are marked as magenta colored circles. The top row of circles represent the diagnostic array A (at about a poloidal index 22) and the lowest row of circles array E (at about a poloidal index 30).

These two plots are the result from the single parameter dependence study, which was described in section 5, showing which diagnostic signal is affected if a specific reconstruction parameter changes. The result of this study is shown for

the total enclosed plasma current (CURTOR) and the plasma pressure profile scale parameter (PRESSCALE) for diagnostics measuring radial magnetic fields. These plots indicate that the diagnostic coils located in array C are particularly sensitive to changes in the total pressure compared to changes in the total enclosed current. The signals of coils in arrays A and E are more determined by the plasma current. Finally the signals in arrays B and D are a linear combination of the plasma pressure and plasma current. The measurements shown in figure 19(*c*) are consistent with the model results from the single parameter dependence study.

9. Conclusions

A new set of magnetic diagnostics has been built, which is optimized to reduce the uncertainty in the plasma current and pressure profiles obtained from plasma equilibrium reconstruction and to draw more accurate conclusions about the

MHD properties in HSX plasmas. A set of 2300 virtual radial, poloidal and helical diagnostic coils in HSX has been used in conjunction with different optimization methods to determine the location of a new array of magnetic diagnostics. A method based on the signal effectiveness has shown specific local regions inside the vessel for magnetic field measurements which can reduce the uncertainty of specific reconstructed plasma quantities. For the plasma energy (integral over the pressure profile) and the total plasma current, local continuous regions have been found for radial and poloidal diagnostic coils, respectively. However, for parameters describing the current and pressure profile, the diagnostic location is not so critical.

Consequently, a study which focuses on diagnostics which undergo a large signal change, caused by a specific change in the equilibrium, has been used to further constrain the possible locations of the new magnetic diagnostics. The results of this method, showing regions with a large signal change, are in agreement with the effective regions from the previous method for parameters describing the total plasma current and plasma energy. However, for parameters describing the profile, a large portion of diagnostics with a high signal effectiveness could be excluded in the design process, since only a small signal change caused by the plasma has been calculated for these diagnostics.

Based on these results and technical limitations, an array of 80 magnetic diagnostics, mainly measuring the poloidal and radial magnetic field, has been built, which could be pre-assembled outside the vessel. This array showed a large reduction in the uncertainty of reconstructed current and pressure profiles compared to a set of existing non-optimized external diagnostics and a set of virtual non-optimized internal diagnostics. Specific coils of this new array have a high sensitivity to either the bootstrap current, which is the dominant source for the toroidal current in HSX, and the Pfirsch–Schlüter current, which has a helical dipole character due to the magnetic field spectrum of HSX. These measurements indicate that it is possible to design local diagnostic coils which are only sensitive to specific plasma equilibrium properties.

This diagnostic optimization has been performed so far for only the quasihelical configuration of HSX at low magnetic beta values. For cases where the magnetic field spectrum changes, because of an increase in beta or with the application of additional auxiliary coils, the Pfirsch–Schlüter and bootstrap current will also change. In such cases, the diagnostic optimization procedure should then consider the change in the plasma equilibrium and the corresponding signal responses. This may include the incorporation of the plasma boundary, along with the plasma pressure and current profiles, into the optimization process.

Acknowledgments

References

[1] de Vries P.C., Johnson M.F., Alper B., Buratti P., Hender T.C., Koslowski H.R., Riccardo V. and JET-EFDA Contributors 2011 *Nucl. Fusion* **51** 053018

[2] Evans T.E. *et al* 2004 *Phys. Rev. Lett.* **92** 235003

[3] Canik J.M. *et al* 2010 *Nucl. Fusion* **50** 034012

[4] Garofalo A.M., Burrell K.H., DeBoo J.C., deGrassie J.S., Jackson G.L., Lanctot M., Reimerdes H., Schaffer M.J., Solomon W.M. and Strait E.J. 2008 *Phys. Rev. Lett.* **101** 195005

[5] Sabbagh S.A. *et al* 2010 *Nucl. Fusion* **50** 025020

[6] Strumberger E., Günter S. and Tichmann C. 2014 *Nucl. Fusion* **54** 064019

[7] Lorenzini R. *et al* 2009 *Nat. Phys.* **5** 570–4

[8] Hanson J.D. *et al* 2013 *Nucl. Fusion* **53** 083016

[9] Hanson J.D., Hirshman S.P., Knowlton S.F., Lao L.L., Lazarus E.A. and Shields J.M. 2009 *Nucl. Fusion* **49** 075031

[10] Hirshman S.P. and Whitson J.C. 1983 *Phys. Fluids* **26** 3553–68

[11] Hirshman S.P., van Rij W.I. and Merkel P. 1986 *Comput. Phys. Commun.* **43** 143–55

[12] Hanson J.D., Knowlton S.F., Stevenson B.A. and Hartwell G.J. 2010 *Contrib. Plasma Phys.* **50** 724–30

[13] Schmitt J.C., Talmadge J.N. and Anderson D.T. 2013 *Nucl. Fusion* **53** 082001

[14] Schmitt J.C., Talmadge J.N., Anderson D.T. and Hanson J.D. 2014 *Phys. Plasmas* **21** 092518

[15] Terranova D., Marrelli L., Hanson J.D., Hirshman S.P., Cianciosa M. and Franz P. 2013 *Nucl. Fusion* **53** 113014

[16] Spong D.A. *et al* 2001 *Nucl. Fusion* **41** 711

[17] Zarnstorff M.C., Weller A., Geiger J., Fredrickson E., Hudson S.R., Knauer J., Reiman A.H., Dinklage A., Fu G.Y. and Ku L.P. 2004 *Proc. 20th Int. Conf. on Fusion Energy* (*Vilamoura, Portugal, 1–6 November 2004*) http://www-naweb.iaea.org/napc/physics/fec/fec2004/datasets/index.html

[18] Lazerson S. and the DIII-D Team 2015 *Nucl. Fusion* **55** 023009

[19] Lazerson S.A., Sakakibara S. and Suzuki Y. 2013 *Plasma Phys. Control. Fusion* **55** 025014

[20] Lazerson S.A. and Chapman I.T. 2013 *Plasma Phys. Control. Fusion* **55** 084004

[21] Pomphrey N., Lazarus E., Zarnstorff M., Boozer A. and Brooks A. 2007 *Phys. Plasmas* **14** 056103

[22] Geiger J., Endler M. and Werner A. 2010 *Contrib. Plasma Phys.* **50** 736–40

[23] Geiger J., Beidler C.D., Drevlak M., Maassberg H., Nührenberg C., Suzuki Y. and Turkin Y. 2010 *Contrib. Plasma Phys.* **50** 770–4

[24] Schmitt J.C. 2011 3D equilibrium reconstruction in the HSX stellarator *PhD Thesis* University of Wisconsin–Madison (http://search.proquest.com/docview/910891771)

[25] Chlechowitz E. 2014 Improved Plasma Equilibrium Reconstruction for the HSX Stellarator using an Optimized Array of Magnetic Coils *PhD Thesis* University of Wisconsin–Madison (http://search.proquest.com/docview/1647451512)

[26] Hirshman S.P., Lazarus E.A., Hanson J.D., Knowlton S.F. and Lao L.L. 2004 *Phys. Plasmas* **11** 595–603